3D Cobalt-MOF/CNF Assemblies as Bifunctional Electrocatalysts for Efficient Water Splitting in Alkaline Media

Abstract

The ultrasonication-assisted synthesis of a three-dimensional Cobalt-MOF/Carbon Nanofiber (Co-MOF/CNF) composite has resulted in an electrocatalyst with exceptional structural stability and efficient charge transfer characteristics. The composite exhibits a remarkably low charge transfer resistance (Rct) of 2 Ω, indicating superior electron conductivity, while a high double-layer capacitance (Cdl) of 12.3 mF/dec enhances its catalytic activity. These properties contribute to its outstanding bifunctional performance in both the hydrogen evolution reaction (HER) and oxygen evolution reaction (OER), achieving low overpotentials of 193 mV and 250 mV, respectively, at a current density of 10 mA/cm². Furthermore, a water-splitting device configured with Co-MOF/CNF electrodes demonstrates efficient overall water electrolysis, requiring only 1.49 V to achieve 10 mA/cm². The system exhibits excellent long-term operational stability, maintaining consistent performance for over 24 hours. These findings highlight the potential of Co-MOF/CNF composites as efficient and durable electrocatalysts for sustainable energy applications.

Introduction:

The recent surge in the consumption and cost of fossil fuels, coupled with their detrimental environmental effects, has underscored the urgent need to explore renewable and sustainable energy sources [1]. Among these, hydrogen has emerged as a promising alternative to conventional fuels due to its eco-friendly nature, high energy density, and ease of storage [2]. Electrochemical water splitting (EWS), encompassing both the oxygen evolution reaction (OER) and hydrogen evolution reaction (HER), represents a viable method for hydrogen production. Nevertheless, this process is hindered by thermodynamic limitations, necessitating the application of additional voltage to overcome these barriers [3].

The mechanisms underlying HER and OER are profoundly influenced by the intrinsic electrochemical and electronic properties of the electrode surface. Enhancing catalytic efficiency requires the optimization of these properties to accelerate sluggish reaction kinetics, which are governed by the catalyst's interaction with water, intermediate species, hydrogen, and oxygen. To facilitate faster reaction kinetics, the development of high-performance

electrocatalytic materials is imperative. Although noble metals and their oxides, such as Pt, RuO_2, and IrO_2, have demonstrated excellent catalytic performance, their limited availability and high cost restrict widespread application [4]. Consequently, research has shifted towards utilizing abundant transition metals as cost-effective alternatives.

Transition metal-based electrocatalysts, including oxides, carbides, nitrides, chalcogenides, and phosphates, have gained considerable attention for their potential in clean hydrogen production through water electrolysis [5]. These materials have shown promise in electrochemical energy conversion and storage devices, such as fuel cells and water electrolyzers, serving as viable substitutes for noble metal-based catalysts [6,7,8].

Commented [A1]: Fokus on Co metal that used in this research. What is the benefit of Co metal among others metal.

Metal-organic frameworks (MOFs) have recently attracted significant interest due to their high porosity, tunable pore structures, large surface areas, and favorable electrochemical properties [9]. MOFs have demonstrated potential across diverse applications, including gas capture, storage, catalysis, sensing, and drug delivery [10]. A notable subclass of MOFs is the zeolitic imidazolate frameworks (ZIFs), composed of metal-imidazole-metal linkages with transition metals like nickel (Ni), cobalt (Co), and zinc (Zn). These materials exhibit complex three-dimensional topologies, resembling the structures of aluminosilicate zeolites [11,12,13].

ZIFs combine the advantageous properties of MOFs and zeolites, such as unimodal microporosity, high crystallinity, ultrahigh surface area, exceptional mechanical stability, and customizable functionalities. Despite these benefits, their direct application in electrochemical processes is limited by poor chemical stability and low electronic conductivity. However, ZIFs are promising precursors for developing metal-carbon composite materials suitable for water splitting due to their high carbon and nitrogen content and rich metal ion composition. These features enhance their reactivity, electron transport capabilities, and stability, making them ideal for electrochemical applications [14,15].

Among ZIFs, ZIF-67, composed of Co^{2+} ions and 2-methylimidazole, exhibits cubic crystal symmetry and has garnered significant attention for water splitting applications due to its structural flexibility and the inherent catalytic activity of cobalt [16]. Co-based catalysts are particularly attractive for OER in alkaline media, owing to their cost-effectiveness, environmental compatibility, and abundant availability. As a result, extensive efforts have been directed towards the synthesis, structural optimization, and in-depth understanding of the structure-property relationships of cobalt-based OER catalysts [17].

However, the poor electronic conductivity of MOFs poses a significant challenge to their overall electrochemical performance. Incorporating carbonaceous materials into MOF structures has proven effective in enhancing their electrochemical efficiency [18]. Various carbon-based materials have been extensively studied as support matrices for active catalytic materials [19,20]. Among these, interwoven hollow one-dimensional (1D) carbon nanofibers (CNFs) offer distinct advantages. Their multichannel hollow architecture facilitates efficient mass and charge transport, thereby accelerating electron transfer processes [21,22]. Additionally, the nanoscale diameter and high aspect ratio of CNFs enable the formation of interconnected three-dimensional networks, promoting mass diffusion and enhancing electrocatalytic performance through improved reaction kinetics [23,24].

In this study, we report the synthesis of a Co-MOF/CNF heterostructure. The Co-MOF was synthesized via a simple solvothermal method using 2-methylimidazole as the organic linker. Subsequently, the Co-MOF was integrated with CNFs through a cost-effective ultrasonication process. The CNFs form a uniform network over the Co-MOF surface, enhancing electrical conductivity and providing additional active sites for ion diffusion, thereby improving electrocatalytic activity. Electrochemical characterization revealed that the Co-MOF/CNF heterostructure functions effectively as a bifunctional catalyst for overall water splitting, exhibiting low overpotentials of 250 mV for OER and 193 mV for HER at a current density of 10 mA/cm^2.

Experimental Section

Commented [A2]: After the Experimental Section, it is suggested to put the Characterization Section, where the section introduces the instrumentation used and their function in this research. State the model and type of instruments.

Synthesis of Co-MOF:

Co-MOF was synthesized via a solvothermal method by dissolving 0.936 g of $Co(NO_3)_2 \cdot 6H_2O$ and 2.5 g of 2-methylimidazole in a solvent mixture of ethanol (30 mL), DMF (20 mL), and water (10 mL). The solution was stirred for 30 minutes, transferred to a 100 mL polymer-coated Teflon-lined autoclave, and heated in a hot air oven for 12 hours. After resting for 24 hours, the product was centrifuged with ethanol, and the resulting powder was dried at 60°C overnight.

Synthesis of Co-MOF/CNF Composite:

The Co-MOF/CNF composite was prepared via ultrasonication. CNFs (0.5 mg/mL) were dispersed in ethanol and sonicated for 1 hour, followed by the addition of 1 mg of Co-MOF. The mixture underwent further ultrasonication for 90 minutes, then was washed with water and ethanol, and dried for future use.

Discussion of results:

The X-ray diffraction (XRD) patterns of Co-MOF and the Co-MOF/CNF composite are presented in Figure 1a. The prominent diffraction peaks for the Co-MOF/CNF composite are observed at 2θ values of 7.1°, 10.2°, 12.5°, 14.5°, 16.4°, 17.9°, 22.0°, 23.3°, 24.5°, 25.5°, and 26.6°, corresponding to the (011), (002), (112), (002), (013), (222), (114), (233), (002), and (134) crystallographic planes, respectively [25]. These diffraction peaks confirm the successful incorporation of Co-MOF within the synthesized composite. Additionally, a low-intensity peak at 2θ = 25.6°, indexed to the (002) plane, signifies carbon nanofibers in the composite [26]. The XRD patterns align with previously reported diffraction data, with minor shifts in positions, suggesting the formation of crystalline MOFs on the surface of CNF.

Commented [A3]: It is suggested to put a result for Co metal and CNF in XRD analysis, FTIR analysis and Raman analysis.

Commented [A4]: Show the peaks in figure 1a

Commented [A5]: Put cited reference to support the statement.

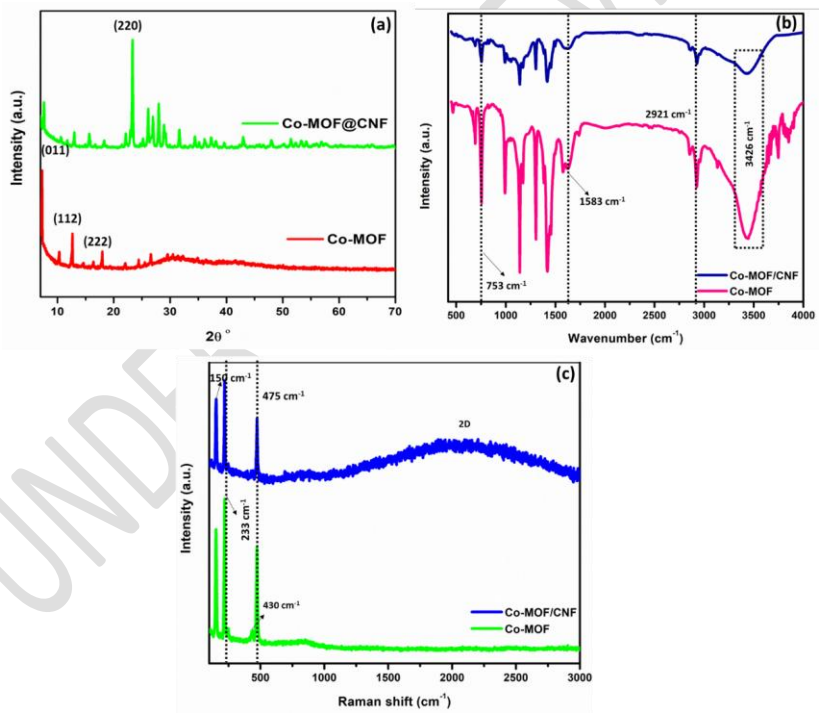

Figure 1: (a) X-ray diffraction patterns, (b) Fourier-transform infrared spectra, and (c) Raman spectra of Co-MOF and Co-MOF/CNF composites

FT-IR spectroscopy was employed to investigate the functional groups present on the surface and to analyze the chemical structural variations among the different catalysts, as illustrated in Figure 1b. The characteristic peak observed in the range of 600–1500 cm^{-1} is attributed to the stretching vibrations of the imidazole ring in Co-MOF. Additionally, the broad absorption band at 3432 cm^{-1} corresponds to the stretching vibrations of N–H and –OH groups [27]. The bending vibration of C=N is responsible for the peak at 753 cm^{-1}, while the absorption bands at 1583 cm^{-1} and 1644 cm^{-1} are assigned to the stretching vibrations of C=N and C=O, respectively [28]. Furthermore, the band at 2921 cm^{-1} indicates C–H stretching vibrations [29]. Variations in the intensity of these peaks suggest effective bonding between CNF and the Co-MOF framework.

Commented [A6]: In Figure 1a, the spectrum shows the value is 3426 cm-1 not 3432 cm-1. Please check.

Raman spectroscopy was conducted to further substantiate the successful integration of CNF into the Co-MOF structure at room temperature, as depicted in Figure 1c. The spectra, recorded in the range of 100–3000 cm^{-1} for both Co–MOF and Co-MOF/CNF, display several low-intensity peaks in the lower Raman shift region at 150, 223, 430, and 475 cm^{-1}, which are associated with the presence of Co ions within the Co-MOF structure [30]. The peaks at 430 and 475 cm^{-1} are attributed to Co–O and Co–N (2-methyl imidazole) bonds within the MOF architecture [31]. Additionally, a prominent peak around 2400 cm^{-1} corresponds to second-order defects (D+G bands), indicating the graphitic characteristics of the Co-MOF/CNF composite [32].

Commented [A7]: In Figure 1c, the Raman spectroscopy shows the value is 233 cm-1 not 233 cm-1. Please check.

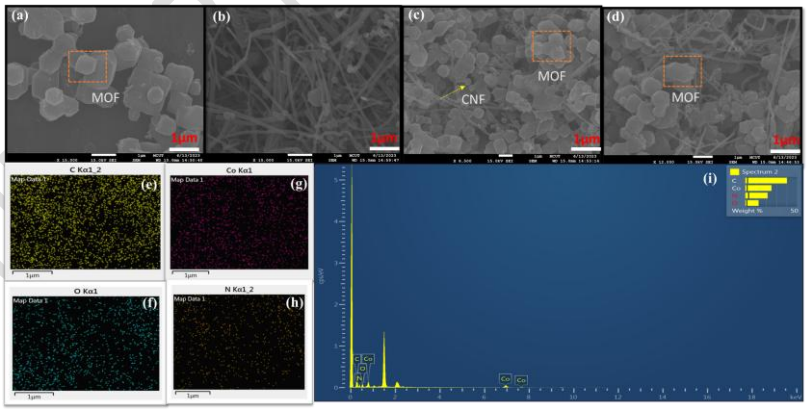

Figure 2: Scanning electron microscopy (SEM) images of (a, b) Co-MOF/CNF composite, (c) Co-MOF, and (d) CNF. (e–h) Energy-dispersive X-ray spectroscopy (EDS) elemental mapping of the Co-MOF/CNF composite, and (i) corresponding EDS spectrum

Commented [A8]: Suggested the sequence of the images should be characterized as for a) Co metal; b) CNF; c) Co-MOF; and d) Co-MOF/CNF.

High-resolution scanning electron microscopy (SEM) was employed to investigate the microstructure and surface characteristics of the Co-MOF/CNF composite. The SEM images of pristine Co-MOF (Figure 2a) illustrate its distinct polyhedral morphology. In contrast, Figure 2b displays the microstructure of CNF at a magnification of 1 µm, highlighting its fibrous network. The SEM analysis of the Co-MOF/CNF composite (Figures 2c and 2d) reveals a complex three-dimensional polyhedral architecture integrated with a network of CNF strands. These high-resolution images provide detailed insights into the surface morphology, showcasing the attachment of Co-MOF onto the CNF framework. The micrographs also illustrate the distribution, size, and spatial arrangement of the MOF structures, offering valuable information regarding the composite's uniformity and homogeneity.

Commented [A9]: the Co metal, CNF, Co-MOF and Co-MOF/CNF composite.

Commented [A10]: In Figure 2 shows a and b for Co-MOF/CNF. Please check.

Commented [A11]: Add the citation to support the statement.

Furthermore, energy-dispersive X-ray spectroscopy (EDS) elemental mapping was conducted to confirm the elemental composition of the Co-MOF composite. The elemental maps (Figures 2e–h) display the distribution of cobalt, carbon, oxygen, and nitrogen, represented by yellow, pink, green, and orange hues, respectively. The corresponding EDS spectrum (Figure 2i) confirms the presence of these key elements, validating the successful synthesis and integration of Co-MOF and CNF within the composite structure.

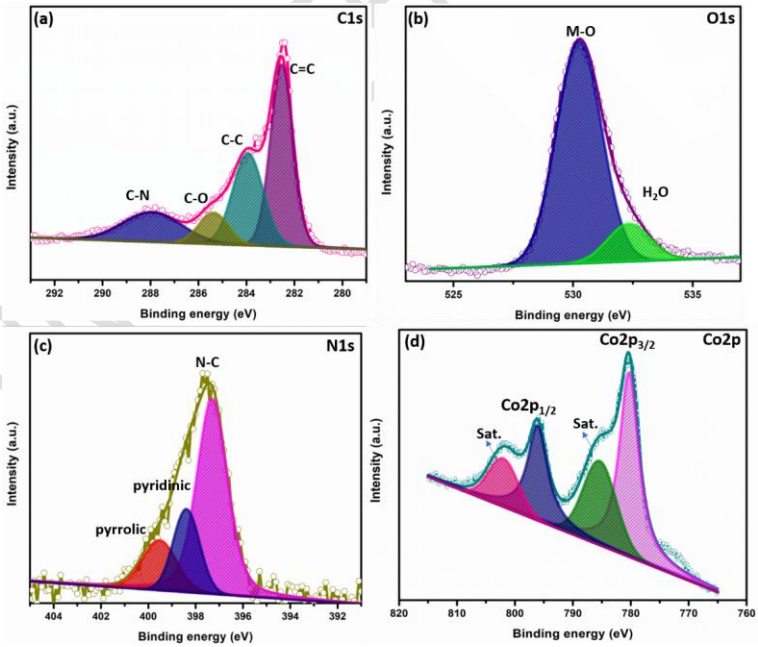

Figure 3: Deconvoluted X-ray photoelectron spectroscopy spectra of (a) C 1s, (b) O 1s, (c) N1s, and (d) Co 2p peaks

.

The C1s high-resolution spectrum (Figure 3a) was deconvoluted to identify various bonding environments, including C-N interactions at 288.0 eV, C-O bonds at 285.4 eV, C-C bonds at 283.9 eV, and C=C bonds at 282.5 eV [33,34]. The O1s spectrum (Figure 3b) exhibits two prominent peaks corresponding to metal-oxygen bonds and adsorbed water molecules, respectively. In the N1s spectrum (Figure 3c), three distinct peaks are observed at binding energies of 397.3 eV, 398.4 eV, and 399.5 eV. The peaks at 398.4 eV and 399.5 eV are attributed to pyridinic and pyrrolic nitrogen species, respectively [35], while the peak at 397.2 eV corresponds to sp2-hybridized nitrogen within a benzene-like structure bonded to carbon atoms [36]. The Co 2p spectrum (Figure 3d) reveals binding energy peaks at 796.1 eV and 780.4 eV, indicative of Co2+ and Co3+ oxidation states, respectively. Additionally, satellite peaks at 785.6 eV and 802.2 eV suggest minor surface oxidation of cobalt species upon exposure to the air atmosphere [37].

Commented [A12]: The Co is binding with which element?

Commented [A13]: superscript

Commented [A14]: superscript

Oxygen evolution reaction:

The oxygen evolution reaction (OER) electrocatalytic performance of the synthesized Co-MOF/CNF was evaluated using a conventional three-electrode setup in a 1 M KOH electrolyte. A uniform catalyst slurry was applied onto a nickel foam (Ni-foam) current collector to facilitate the measurements. Linear sweep voltammetry (LSV) was employed to assess the OER activity of the Co-MOF/CNF electrocatalyst. As illustrated in Figure 4a, the Co-MOF/CNF exhibited a significantly lower overpotential of 250 mV at a current density of 10 mA/cm² compared to Co-MOF (300 mV), CNF (340 mV), and bare Ni-foam (390 mV), demonstrating superior OER activity. The Tafel slope, which reflects the electrocatalytic kinetics during the OER process, revealed that a lower value corresponds to enhanced catalytic efficiency.

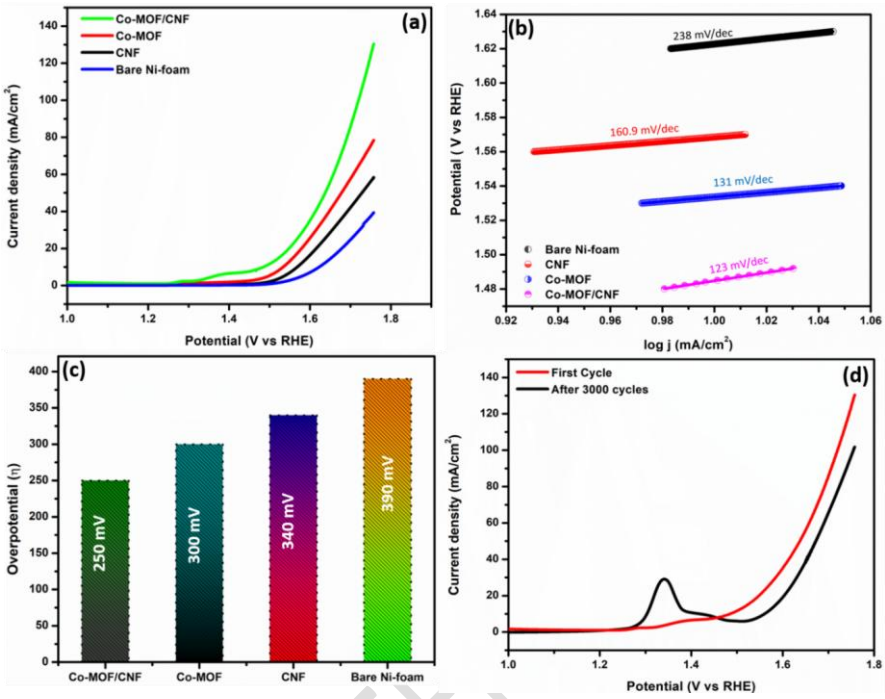

Figure 4: (a) Linear sweep voltammetry (LSV) polarization curves recorded in 1 M KOH at a scan rate of 10 mV/s for Co-MOF/CNF, Co-MOF, CNF, and bare Ni-foam electrodes; (b) corresponding Tafel plots; (c) comparison of overpotentials for the synthesized catalysts; and (d) LSV curves of Co-MOF/CNF before and after durability testing over 3000 cyclic voltammetry (CV) cycles at 50 mV/s

Compared to the Tafel slopes of Co-MOF (131 mV/dec), CNF (160.9 mV/dec), and bare Ni-foam (238 mV/dec) electrodes, the Co-MOF/CNF electrode exhibits a significantly lower Tafel slope, indicating superior kinetics conducive to the oxygen evolution reaction (OER), as illustrated in Figure 4b. The Co-MOF/CNF composite demonstrates both a remarkably low overpotential and a reduced Tafel slope, signifying enhanced OER efficiency. The oxygen evolution overpotentials (η) at a current density of 10 mA/cm^2 for Co-MOF/CNF, Co-MOF, CNF, and bare Ni-foam electrodes were determined, as presented in Figure 4c.

The enhanced electrochemical performance is attributed to the synergistic interaction between Co-MOF and CNF within the composite. The incorporation of cobalt within the imidazole framework introduces porosity, which enhances the catalyst's surface area and facilitates charge

transfer. Additionally, the nitrogen atoms embedded in the MOF framework act as secondary active sites for electrocatalysis. Due to nitrogen's higher electronegativity, it modifies the charge densities of adjacent carbon atoms, thereby lowering the adsorption free energy ($\Delta G(H^*)$) and promoting the adsorption of OER intermediates, ultimately enhancing catalytic activity [38].

Considering that OER involves a complex four-electron/four-proton transfer process, it generally requires a higher overpotential compared to the hydrogen evolution reaction (HER). Moreover, most OER catalysts derived from earth-abundant materials exhibit limited stability in acidic environments. Based on these considerations, alkaline media are deemed more favorable for achieving higher overall water-splitting efficiency compared to acidic or neutral conditions.

A proposed mechanism for the OER in an alkaline medium is outlined as follows:

$$Co + OH^- \longrightarrow Co\text{-}OH + e^-$$

$$Co\text{-}OH + OH^- \longrightarrow Co\text{-}O + H_2O + e^-$$

$$Co\text{-}O + OH^- \longrightarrow Co\text{-}OOH + e^-$$

$$Co\text{-}OOH + OH^- \longrightarrow Co + O_2 + H_2O + e^-$$

Another contributing factor to the enhanced electrocatalytic performance is the nickel foam substrate. Its macroporous architecture and excellent electrical conductivity facilitate efficient charge transfer across the electrode and promote effective mass transport of electrolytes and the generated gas bubbles (H_2 and O_2) [39].

Moreover, XPS analysis confirms the presence of graphitic, pyridinic, and metal-coordinated nitrogen species within the Co-MOF/CNF catalyst, which are recognized as additional active sites for the oxygen evolution reaction (OER). As illustrated in Figure 4d, the linear sweep voltammetry (LSV) curve obtained after 3000 cycles of cyclic voltammetry at a scan rate of 50 mV/s exhibits noticeable changes compared to the initial data, likely due to the oxidation of nickel. Despite these changes, the Co-MOF/CNF catalyst demonstrates exceptional stability, with its overpotential shifting slightly from an onset potential of 1.47 V to 1.53 V (vs. RHE) after 3000 cycles.

Commented [A15]: shorten the arrow length (use arrow symbol)

Hydrogen evolution reaction:

The electrocatalytic HER behaviour of Co-MOF, CNF, Co-MOF/CNF, and bare Ni-foam was investigated in a typical three-electrode setup with a scan rate of 10 mV/s in 1 M KOH solution.

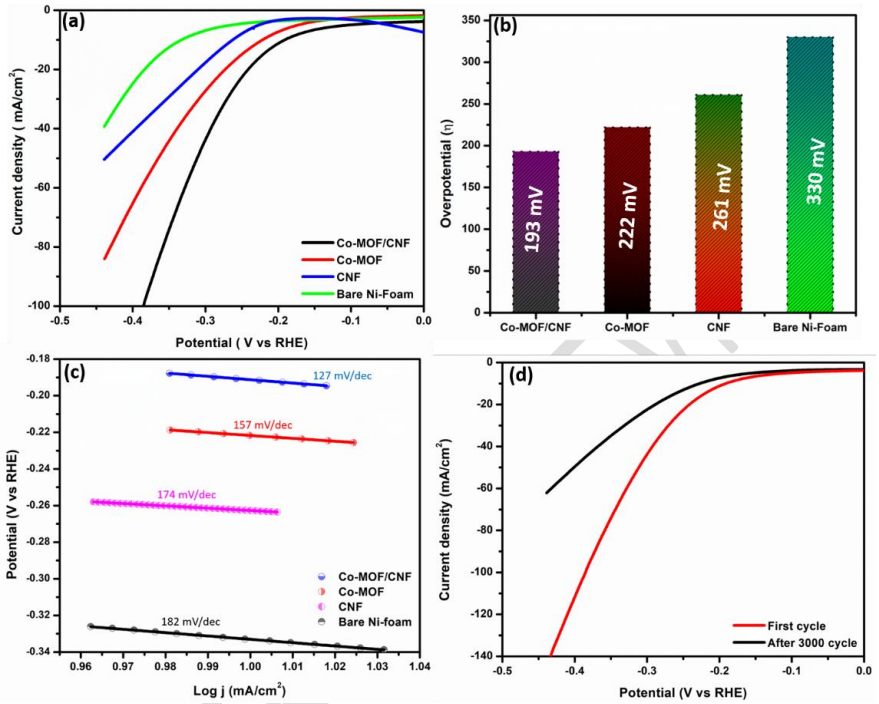

Figure 5: (a) Linear sweep voltammetry (LSV) polarization curves measured in 1 M KOH at a scan rate of 10 mV/s, (b) comparison of overpotentials among various catalysts, and (c) LSV curves obtained before and after durability testing over 3000 cyclic voltammetry (CV) cycles at 50 mV/s.

The Co-MOF/CNF composite was deposited onto nickel foam and utilized as the working electrode. As shown in Figure 5a, the LSV curves reveal that Co-MOF/CNF requires an overpotential of 193 mV to achieve a stable current density of 10 mA/cm². The overpotentials for Co-MOF, CNF, and bare Ni-foam were found to be 222, 261, and 330 mV, respectively. Figure 5b presents the computed hydrogen evolution overpotentials (η) at a current density of 10 mA/cm² for the Co-MOF/CNF, Co-MOF, CNF, and bare Ni-foam electrodes. It is believed that the synergistic interaction between nitrogen and cobalt species optimizes the electronic structure of carbon and enhances the energy of hydrogen atom adsorption on carbon, thereby

improving catalysis and electron transfer during the HER process. The corresponding Tafel plots in Figure 5c, generated by linear fitting, were used to evaluate the HER kinetics of Co-MOF, Co-MOF/CNF, CNF, and bare Ni-foam. The Tafel slope for Co-MOF/CNF is 127 mV/dec, which is smaller than the slopes for Co-MOF, CNF, and bare Ni-foam (157, 174, and 182 mV/dec, respectively). This suggests that Co-MOF/CNF facilitates HER via the Volmer-Heyrovsky combination mechanism, with desorption being the rate-determining step. In alkaline solutions, the Volmer step involves water dissociation and subsequent hydrogen reduction and adsorption (H_2O + e- → Hads + OH^-), followed by either the Heyrovsky step (Hads + H_2O + e^- → H_2 + OH^-) or the Tafel step (2Hads → H_2). These results underscore the superior catalytic performance of Co-MOF/CNF, demonstrating that structural engineering can enhance both electron transfer efficiency and active site accessibility, which are critical for improving electrocatalytic activity. Stability, which refers to both material durability and sustained hydrogen evolution activity, was evaluated through prolonged CV cycling at a scan rate of 50 mV/s for 3000 cycles. The Co-MOF/CNF composite exhibited minimal deviation in the LSV curves (Figure 5d), indicating excellent stability.

Commented [A16]: subscript

Commented [A17]: subscript

Commented [A18]: subscript

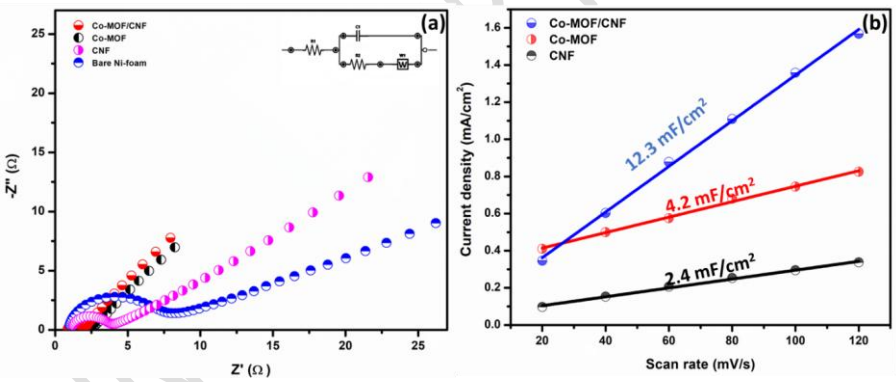

Figure 6: (a) Electrochemical impedance spectroscopy (EIS) spectra of Co-MOF/CNF, Co-MOF, CNF, and bare Ni-foam electrodes, and (b) plot of Δj (current density difference) as a function of varying scan rates.

Electrochemical impedance spectroscopy (EIS) measurements were conducted in 1 M KOH using both Co-MOF and Co-MOF/CNF electrodes within the frequency range of 100 kHz to 0.1 Hz, as depicted in Figure 6a. A lower charge transfer resistance (Rct) is indicative of enhanced water-splitting performance, as it facilitates faster charge transfer and more favorable reaction kinetics [42]. The Nyquist plot reveals that Co-MOF/CNF exhibits an Rct of 2 Ω,

which is lower than that of Co-MOF (2.37 Ω), CNF (4.8 Ω), and bare Ni-foam (9.6 Ω). The smallest semicircle diameter observed for Co-MOF/CNF signifies the highest electron transfer rate among the catalysts during the OER process, directly contributing to superior catalytic activity. The incorporation of carbon nanofibers significantly improves the composite's conductivity, thereby accelerating electron migration. These findings suggest that the integration of CNF into the Co-MOF framework positively influences electron transport properties.

Additionally, the electrochemical surface area (ECSA) of the catalysts was determined through the calculation of electrochemical double-layer capacitance (Cdl) [43]. As expected, Co-MOF/CNF exhibits the highest capacitance, reflecting the presence of abundant active sites critical for enhanced catalytic performance. The Cdl values obtained from the slope of the linear plot of current density versus scan rate for Co-MOF, CNF, and Co-MOF/CNF are approximately 4.2, 2.4, and 12.3 mF/cm², respectively, as shown in Figure 6c. Despite a relatively lower ECSA, the Co-MOF/CNF composite demonstrates superior catalytic performance compared to Co-MOF, CNF, and bare Ni-foam, which can be attributed to the high intrinsic activity of the Co^{2+} active sites. The superior ECSA of the Co-MOF/CNF catalyst likely results from the uniform distribution of CNF across the hexagonal Co-MOF structure, effectively exposing more active sites for catalytic reactions.

Commented [A19]: Add citation to support the statement.

Overall water splitting:

The synthesized Co-MOF/CNF composite exhibits remarkable electrocatalytic performance for both the hydrogen evolution reaction (HER) and oxygen evolution reaction (OER), highlighting its potential as a bifunctional catalyst for efficient overall water splitting. To evaluate this, a two-electrode system was constructed using the Co-MOF/CNF composite (Figure 7). Notably, this alkaline electrolyzer achieved low operating voltages of 1.49 V for HER and 1.83 V for OER (Figure 7a), while delivering current densities of 10 and 50 mA/cm^2, respectively.

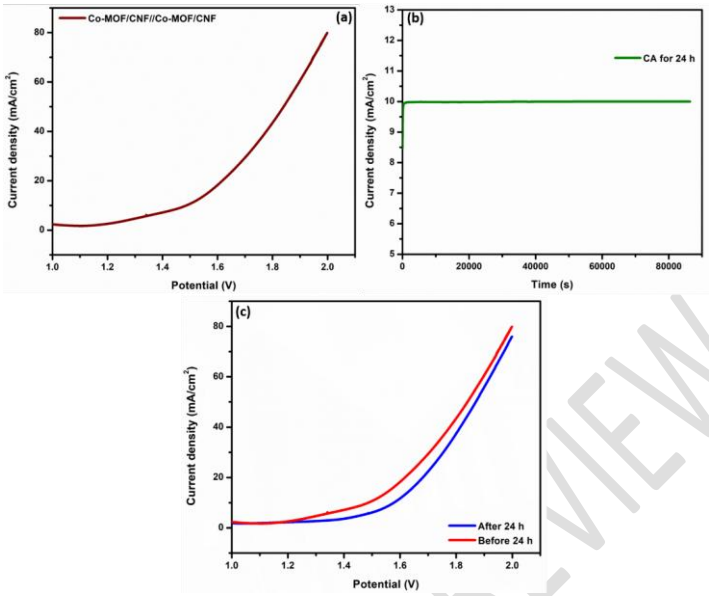

Figure 7: (a) Linear sweep voltammetry (LSV) curves obtained at a scan rate of 10 mV/s, (b) Chronoamperometry (CA) stability test performed at a current density of 10 mA/cm^2, and (c) LSV curves recorded after the stability test, evaluating overall water-splitting activity in an electrolysis cell with Co-MOF/CNF as both the anode and cathode in a 1 M KOH solution.

The durability of the water electrolyzer was evaluated at a current density of 10 mA/cm² (Figure 7b), with electrolysis operations sustained for over 24 hours, demonstrating the catalyst's remarkable stability for overall water splitting. Linear sweep voltammetry (LSV) results were analyzed for the composites before and after chronoamperometry, as illustrated in Figure 7c.

Based on the aforementioned evaluations and electrochemical analyses, several factors are identified as contributors to the enhanced electrocatalytic performance of the Co-MOF/CNF composite:

(i) The three-dimensional porous structure of Co-MOF offers a high density of catalytic active sites, promoting the adsorption of hydrogen- and oxygen-containing intermediates, thereby improving both hydrogen and oxygen evolution reactions.

(ii) The incorporation of CNF into the MOF alters the surface morphology of Co-MOF, which enhances the activation energy of reactants during adsorption and desorption processes on the catalyst surface, significantly boosting catalytic efficiency.

(iii) The presence of CNF within the Co-MOF catalyst matrix enhances the composite's electrical conductivity, facilitating improved energy and mass transfer at the electrode/electrolyte interface, thus accelerating the kinetics of both the hydrogen evolution reaction (HER) and oxygen evolution reaction (OER).

Conclusion:

The findings of this study emphasize the potential of three-dimensional Co-MOF/CNF microstructured assemblies as promising candidates for use in alkaline water electrolyzers. The catalyst's physical properties were thoroughly examined using appropriate analytical techniques. Additionally, electrochemical performance was assessed through various methods, including Tafel slope analysis, Electrochemical Impedance Spectroscopy (EIS), Linear Sweep Voltammetry (LSV), and Cyclic Voltammetry (CV). These analyses provided a comprehensive evaluation of the catalyst's structural and electrochemical characteristics. The results demonstrate that the Co-MOF/CNF composite exhibits superior performance in an alkaline environment, with lower overpotentials of 250 mV for the OER and 193 mV for the HER. The combination of CNF and Co-MOF offers a large active surface area, which enhances charge transfer and catalytic stability. Furthermore, the catalyst's activity was evaluated for overall water splitting, where the Co-MOF/CNF composite achieved remarkable performance, delivering 1.49 V at a current density of 10 mA/cm^2 in alkaline conditions. These findings highlight the critical role of synergistic material integration in achieving enhanced electrocatalytic performance and advancing water-splitting technologies. This research opens new avenues for the development of innovative catalytic materials, with significant implications for addressing global energy and environmental challenges as the search for cleaner and more efficient energy conversion solutions continues.

References:

1. Zeng Y-T, Xu M-Y, Wang T, et al (2023) Ru-decorated cobalt-iron oxide nanosheet arrays derived from MOF and LDH double-precursors for overall water splitting in alkali and seawater. Electrochim Acta 444:142004. https://doi.org/https://doi.org/10.1016/j.electacta.2023.142004.
2. Wu Z, Liu B, Jing H, et al (2023) Porous carbon framework decorated with carbon nanotubes encapsulating cobalt phosphide for efficient overall water splitting. J Colloid Interface Sci 629:22–32. https://doi.org/https://doi.org/10.1016/j.jcis.2022.08.102.

3. Gautam J, Chanda D, Mekete Meshesha M, et al (2023) Manganese cobalt sulfide/molybdenum disulfide nanowire heterojunction as an excellent bifunctional catalyst for electrochemical water splitting. J Colloid Interface Sci 638:658–671. https://doi.org/https://doi.org/10.1016/j.jcis.2023.02.029.
4. Tian R, Wang F, Zou C, et al (2023) Modulating organic ligands to construct 2D–3D-hybrid porous P-doped metal-organic frameworks electrocatalyst for overall water splitting. J Alloys Compd 933:167670. https://doi.org/https://doi.org/10.1016/j.jallcom.2022.167670.
5. Ali M, Pervaiz E, Rabi O (2021) Enhancing the Overall Electrocatalytic Water-Splitting Efficiency of Mo2C Nanoparticles by Forming Hybrids with UiO-66 MOF. ACS Omega 6:34219–34228. https://doi.org/10.1021/acsomega.1c03115.
6. Rajagopal K, Suresh P, Rajaram A, Natarajan A (2023) A novel Co-precipitation assisted Li1.05Ni0.5Mn1.40Ce0.10O4 spinel as an eloquent electrocatalyst for methanol oxidation. Chem Phys Lett 823:140518. https://doi.org/https://doi.org/10.1016/j.cplett.2023.140518.
7. Rajagopal K, Kathiresan M, Rajaram A, Natarajan A (2023) Development of robust noble-metal free lanthanum, neodymium doped Li1.05Ni0.5Mn1.5O4 as a bifunctional electrocatalyst for electrochemical water splitting. RSC Adv 13:23829–23840. https://doi.org/10.1039/D3RA04495E
8. Suresh P, Natarajan A, Rajaram A (2024) Multi-Active Sites Loaded NiCu-MOF@MWCNTs as a Bifunctional Electrocatalyst for Electrochemical Water Splitting Reaction. Langmuir 40:9509–9519. https://doi.org/10.1021/acs.langmuir.4c00054
9. Strauss V, Margraf JT, Dirian K, et al (2015) Carbon Nanodots: Supramolecular Electron Donor-Acceptor Hybrids Featuring Perylenediimides. Angew Chemie - Int Ed 54:8292–8297. https://doi.org/10.1002/anie.201502482.
10. Pavithra S, Jothi VK, Rajaram A, et al (2022) A Facile Synthesis of a Fusiform-Shaped Three-Dimensional Co/Mn@CNDs-MOF Nanocomposite as an Efficient Electrocatalyst for Oxygen Evolution Reaction in Alkaline Medium. Energy and Fuels 36:6409–6419. https://doi.org/10.1021/acs.energyfuels.2c00780.
11. Wang Z, Wang Z, Wang J, et al (2023) Ni, Zn Co-doping ZIF-67-derived electrocatalyst based on CNT film for efficient overall water splitting. Int J Hydrogen Energy 48:29189–29197. https://doi.org/https://doi.org/10.1016/j.ijhydene.2023.04.082.

12. Du X, Ding Y, Zhang X (2023) MOF-derived Zn–Co–Ni sulfides with hollow nanosword arrays for high-efficiency overall water and urea electrolysis. Green Energy Environ 8:798–811. https://doi.org/https://doi.org/10.1016/j.gee.2021.09.007.
13. Vílchez-Cózar Á, Armakola E, Gjika M, et al (2022) Exploiting the Multifunctionality of M2+/Imidazole–Etidronates for Proton Conductivity (Zn2+) and Electrocatalysis (Co2+, Ni2+) toward the HER, OER, and ORR. ACS Appl Mater Interfaces 14:11273–11287. https://doi.org/10.1021/acsami.1c21876.
14. Shahsavari M, Mohammadzadeh Jahani P, Sheikhshoaie I, et al (2022) Green Synthesis of Zeolitic Imidazolate Frameworks: A Review of Their Characterization and Industrial and Medical Applications. Materials (Basel).
15. Huang X-C, Lin Y-Y, Zhang J-P, Chen X-M (2006) Ligand-Directed Strategy for Zeolite-Type Metal–Organic Frameworks: Zinc(II) Imidazolates with Unusual Zeolitic Topologies. Angew Chemie Int Ed 45:1557–1559. https://doi.org/https://doi.org/10.1002/anie.200503778.
16. Li J, Ge R, Li Y, et al (2022) Zeolitic imidazolate framework-67 derived cobalt-based catalysts for water splitting. Mater Today Chem 26:101210. https://doi.org/https://doi.org/10.1016/j.mtchem.2022.101210.
17. Tripathy RK, Samantara AK, Behera JN (2019) A cobalt metal–organic framework (Co-MOF): a bi-functional electro active material for the oxygen evolution and reduction reaction. Dalt Trans 48:10557–10564. https://doi.org/10.1039/C9DT01730E.
18. Yan Y, Lin X, Ge J, Li X (2023) Conductive metal-organic frameworks with wheel-shaped metallomacrocycle subunits as high-performance supercapacitor electrodes. Chem Eng J 468:143739. https://doi.org/https://doi.org/10.1016/j.cej.2023.143739.
19. Murugan K, Jothi VK, Rajaram A, Natarajan A (2022) Novel Metal-Free Fluorescent Sensor Based on Molecularly Imprinted Polymer N-CDs@MIP for Highly Selective Detection of TNP. ACS Omega 7:1368–1379. https://doi.org/10.1021/acsomega.1c05985
20. Komal M, Vinoth Kumar J, Arulmozhi R, et al (2023) Selective and sensitive on-site colorimetric detection of 4{,}4′-isopropylidenediphenol using non-enzymatic molecularly imprinted graphitic carbon nitride hybrids in milk and water samples. New J Chem. https://doi.org/10.1039/D3NJ01241G
21. Murugan K, Natarajan A (2024) A novel N-CNDs/PAni modified molecular imprinted polymer for ultraselective and sensitive detection of ciprofloxacin in lentic ecosystems: a dual responsive optical sensor. Anal Methods. https://doi.org/10.1039/D4AY00323C

Commented [A20]: superscript

Commented [A21]: superscript

Commented [A22]: superscript

22. Ahmad MW, Choudhury A, Dey B, et al (2022) Three-dimensional core-shell niobium-metal organic framework@carbon nanofiber mat as a binder-free positive electrode for asymmetric supercapacitor. J Energy Storage 55:105484. https://doi.org/https://doi.org/10.1016/j.est.2022.105484.
23. Tian D, Song N, Zhong M, et al (2020) Bimetallic MOF Nanosheets Decorated on Electrospun Nanofibers for High-Performance Asymmetric Supercapacitors. ACS Appl Mater Interfaces 12:1280–1291. https://doi.org/10.1021/acsami.9b16420.
24. Sun L, Xu H, Yang Y, et al (2023) Graphitic carbon-encapsulated cobalt nanoparticles embedded 1D porous hollow carbon nanofibers as advanced multifunctional electrocatalysts for overall water splitting and Zn-air batteries. Int J Hydrogen Energy 48:5095–5106. https://doi.org/https://doi.org/10.1016/j.ijhydene.2022.11.058.
25. Lee Y-R, Yoo H, Choi J, Ahn W-S (2020) Electrocatalytic oxygen reduction over Co@Co3O4/N-doped porous carbon derived from pyrolysis of ZIF-8/67 on cellulose nanofibers. Cellulose 27:2723–2735. https://doi.org/10.1007/s10570-019-02937-5.
26. Sundriyal S, Shrivastav V, Kaur H, et al (2018) High-Performance Symmetrical Supercapacitor with a Combination of a ZIF-67/rGO Composite Electrode and a Redox Additive Electrolyte. ACS Omega 3:17348–17358. https://doi.org/10.1021/acsomega.8b02065.
27. Truong T, Hoang TM, Nguyen CK, et al (2015) Expanding applications of zeolite imidazolate frameworks in catalysis: Synthesis of quinazolines using ZIF-67 as an efficient heterogeneous catalyst. RSC Adv 5:24769–24776. https://doi.org/10.1039/c4ra16168h.
28. Manimohan M, Pugalmani S, Ravichandran K, Sithique MA (2020) Synthesis and characterisation of novel Cu(ii)-anchored biopolymer complexes as reusable materials for the photocatalytic degradation of methylene blue. RSC Adv 10:18259–18279. https://doi.org/10.1039/D0RA01724H.
29. Hadjiivanov KI, Panayotov DA, Mihaylov MY, et al (2021) Power of Infrared and Raman Spectroscopies to Characterize Metal-Organic Frameworks and Investigate Their Interaction with Guest Molecules. Chem Rev 121:1286–1424. https://doi.org/10.1021/acs.chemrev.0c00487.
30. Hoa DTN, Tu NTT, Son LVT, et al (2021) Electrochemical Determination of Diclofenac by Using ZIF-67/*g*-C_3N_4 Modified Electrode. Adsorpt Sci Technol 2021:7896286. https://doi.org/10.1155/2021/7896286.

31. Azizzadeh A, Amooey AA, Ghasemi S (2022) Ternary metal-organic framework/multi-walled carbon nanotube/iron oxide nanocomposite for removal of butachlor pesticide. Environ Sci Eur 34:49. https://doi.org/10.1186/s12302-022-00627-x.
32. Ma B, Rodriguez RD, Ruban A, et al (2019) The correlation between electrical conductivity and second-order Raman modes of laser-reduced graphene oxide. Phys Chem Chem Phys 21:10125–10134. https://doi.org/10.1039/C9CP00093C.
33. Dolgov A, Lopaev D, Lee CJ, et al (2015) Characterization of carbon contamination under ion and hot atom bombardment in a tin-plasma extreme ultraviolet light source. Appl Surf Sci 353:708–713. https://doi.org/https://doi.org/10.1016/j.apsusc.2015.06.079.
34. Chen Q, Gao G, Zhang Y, et al (2021) Dual functions of CO2 molecular activation and 4f levels as electron transport bridges in erbium single atom composite photocatalysts therefore enhancing visible-light photoactivities. J Mater Chem A 9:15820–15826. https://doi.org/10.1039/D1TA02926F.
35. Qi X, Tian H, Dang X, et al (2019) A bimetallic Co/Mn metal–organic-framework with a synergistic catalytic effect as peroxidase for the colorimetric detection of H2O2. Anal Methods 11:1111–1124. https://doi.org/10.1039/C8AY02514B.
36. Tian K, Wang J, Cao L, et al (2020) Single-site pyrrolic-nitrogen-doped sp2-hybridized carbon materials and their pseudocapacitance. Nat Commun 11:3884. https://doi.org/10.1038/s41467-020-17727-y.
37. Tan BJ, Klabunde KJ, Sherwood PMA (1991) XPS studies of solvated metal atom dispersed (SMAD) catalysts. Evidence for layered cobalt-manganese particles on alumina and silica. J Am Chem Soc 113:855–861. https://doi.org/10.1021/ja00003a019.
38. Perivoliotis DK, Ekspong J, Zhao X, et al (2023) Recent progress on defect-rich electrocatalysts for hydrogen and oxygen evolution reactions. Nano Today 50:101883. https://doi.org/https://doi.org/10.1016/j.nantod.2023.101883.
39. Pavithra S, Komal M, Rajaram A, et al (2023) Conducting polymer encrusted Cu / Mn-MOF-CNDs: A facile synthesis, characterization and its hydrogen evolution activity in alkaline media and seawater. Synth Met 297:117422. https://doi.org/10.1016/j.synthmet.2023.117422.
40. Gao X, Deng H, Dai Q, et al (2022) Smart Designs of Mo Based Electrocatalysts for Hydrogen Evolution Reaction. Catalysts 12
41. Jovanović AZ, Bijelić L, Dobrota AS, et al (2022) Enhancement of hydrogen evolution reaction kinetics in alkaline media by fast galvanic displacement of nickel with rhodium

– From smooth surfaces to electrodeposited nickel foams. Electrochim Acta 414:1–27. https://doi.org/10.1016/j.electacta.2022.140214.

42. Zhang W, Zheng J, Gu X, et al (2019) Facile synthesis, characterization and DFT studies of a nanostructured nickel–molybdenum–phosphorous planar electrode as an active electrocatalyst for the hydrogen evolution reaction. Nanoscale 11:9353–9361. https://doi.org/10.1039/C8NR08039A.
43. Shin J, Guo J, Zhao T, Guo Z (2019) Functionalized Carbon Dots on Graphene as Outstanding Non-Metal Bifunctional Oxygen Electrocatalyst. Small 15:1–9. https://doi.org/10.1002/smll.201900296